Journal of the Mechanical Behavior of Biomedical Materials 180 (2026) 107481

Contents lists available at ScienceDirect

Journal of the Mechanical Behavior of Biomedical Materials

journal homepage: www.elsevier.com/locate/jmbbm

Aging reduces strain magnitude and heterogeneity while increasing apparent stiffness of the rat proximal tibia

Laura Müller [a], Sriram Kunnoth [b], Hajar Souhail [a], Margaux Ska [c], Piyush Uniyal [d], Luca D'Andrea [e], Pasquale Vena [e], G Harry van Lenthe [d], Enrico Dall'Ara [b,1], Davide Ruffoni [a,*,1]

[a] Mechanics of Biological and Bioinspired Materials Laboratory, Department of Aerospace and Mechanical Engineering, University of Liège, Liège, Belgium
[b] Insigneo Institute, Division of Clinical Medicine, School of Medicine & Population Health, University of Sheffield, Sheffield, UK
[c] Microfluidic Laboratory, Department of Aerospace and Mechanical Engineering, University of Liège, Liège, Belgium
[d] Department of Mechanical Engineering, KU Leuven, Leuven, Belgium
[e] Laboratory of Biological Structure Mechanics (LaBS) - Department of Chemistry, Materials and Chemical Engineering "Giulio Natta", Politecnico di Milano, Milan, Italy

ARTICLE INFO

Keywords:
Osteochondral junction
Epiphysis
Knee
Aging
Strain distribution
Image-based finite element analysis
Digital volume correlation

ABSTRACT

The epiphyses of long bones play a critical role in joint integrity by absorbing and redistributing joint forces. While aging induces microstructural and material changes in this anatomical site, their impact on the internal mechanical environment of the epiphysis remains poorly characterized. In this study, we quantified age-related alterations in epiphyseal strain distribution in the knee joints of adult and aged male Wistar rats using in situ mechanical testing combined with micro-computed tomography, digital volume correlation, and finite element analysis. Aging was associated with a pronounced reduction in deformation: mean compressive and tensile principal strains in aged animals decreased by approximately 63% and 67%, respectively, compared with strains in adult animals. In addition to reduced strain magnitude, aged epiphyses exhibited less heterogeneous strain distributions, altered spatial strain patterns, and increased inter-individual variability of the deformation. These mechanical changes are consistent with previously reported age-related thickening of the subchondral bone plate, trabecular coarsening, and increased tissue mineralization. Together, these findings demonstrate that aging leads to substantial stiffening of the proximal tibia and alters its behavior under compression. Such changes may affect the protective mechanical function of the epiphysis and contribute to an unfavorable mechanical environment for articular cartilage, which may predispose to joint degeneration.

1. Introduction

The knee joint is a sophisticated biomechanical system enabling precise movements while providing mechanical stability and shock absorption during locomotion. These multiple functions depend on several components working together, including soft tissues (articular cartilage, ligaments, meniscus, and growth plate), hard tissues (mineralized cartilage and bone), and even a liquid (synovial fluid). Spanning a region from the articular cartilage to the growth plate, the end of a long bone (named epiphysis) plays an essential role in maintaining joint integrity: it attenuates contact stresses, provides a proper foundation for articular cartilage, and ensures load redistribution across the joint, thereby protecting the overlying cartilage and the underlying metaphyseal bone (Radin and Rose, 1986; Pugh et al., 1973; Lotz et al., 1991). From a structural viewpoint, the epiphysis encompasses tissues with highly dissimilar mechanical and functional properties, including articular and mineralized cartilage, the subchondral bone plate, the subchondral trabecular network, and the growth plate.

This region is of high clinical relevance as subjected to age-related changes that can lead to degeneration and diseases such as osteoarthritis (OA), the most common chronic joint disorder. While the extent of the age-related changes varies between species and anatomical location (Ren et al., 2018; Ries et al., 2020; Goliath et al., 2022), some general features can be identified. For instance, in humans, the growth plate cartilage is replaced by bone during late adolescence, leading to growth plate fusion; conversely, in rodents and other small mammals,

* Corresponding author. University of Liege Quartier Polytech 1 Allée de la Découverte 9, B-4000, Liège. Belgium.
E-mail address: druffoni@uliege.be (D. Ruffoni).
[1] Equal supervision of the work.

https://doi.org/10.1016/j.jmbbm.2026.107481
Received 25 February 2026; Received in revised form 27 April 2026; Accepted 27 May 2026
Available online 27 May 2026

the growth plate usually does not close completely until death (Ağırdil, 2020; Haimov et al., 2020). During aging, articular cartilage tends to become thinner and shows several compositional modifications, including a decrease in proteoglycan content and altered collagen structure, leading to loss of elasticity (Lotz and Loeser, 2012). Particularly critical are also alterations in subchondral bone, such as thickening of the subchondral plate (i.e., a region beneath articular cartilage including mineralized cartilage and cortical bone) and of the underlying trabeculae (Ren et al., 2018; Yamada et al., 2002), those changes are driven by subchondral bone remodeling (Li et al., 2015). Also, the thin layer of mineralized cartilage, sandwiched between articular cartilage and subchondral bone, shows the signature of aging: in a previous work, we found a significant increase in mineral content and elastic modulus in aged rats compared to adult rats, together with a disruption in the gradient at the interface between unmineralized and mineralized cartilage (Müller et al., 2026). All these modifications may contribute to increased joint stiffness and reduced energy absorption, leading to a higher risk of joint degenerative diseases.

While there is interest in understanding how age-related alterations can modify the load transfer across the joint, little is known about the specific deformation field in the epiphysis when subjected to external loads. Understanding the mechanical environment within the epiphysis is highly relevant for comprehending the mechanisms behind age-related joint degeneration. Yet, this assessment remains challenging due to the intricate architecture and the presence of multiple interacting tissues. A powerful approach that enables the mechanical characterization of such a complicated heterogeneous region combines mechanical testing, X-ray tomography (typical micro-CT or nano-CT), and digital volume correlation (DVC), allowing to measure internal displacements and strains (Tozzi and Dall'Ara, 2025; Dall'Ara and Tozzi, 2022). Briefly, DVC relies on the elastic registration of pairs of three-dimensional images, captured in undeformed and deformed configurations, to find the displacement field, which is then derived into strains (Dall'Ara and Tozzi, 2022; Roberts et al., 2014; Palanca et al., 2015). This method inherently accounts for sample size, shape, morphology, microstructure, and material heterogeneity. It also allows for the application of loading conditions that mimic the complex loading at the joint (Peña Fernández et al., 2020; Madi et al., 2020). Image-based micro-structural finite element analysis (micro-FE) is another technique widely used to characterize the mechanical behavior of bones under different loading scenarios, taking into account fine microstructural details (Ruffoni and van Lenthe, 2017; Namiranian et al., 2025; van Rietbergen and Ito, 2015). Micro-FE can be considered complementary to DVC as it gives insight into the stress field and can be used to test the specific impact of material properties independent of microstructure (Gross et al., 2012; Renders et al., 2008, 2011). Micro-FE and DVC predictions can not only be compared (Zauel et al., 2005) but also combined, for example, to validate micro-FE models (Costa et al., 2017).

Focusing on DVC, this method has been used to study the local tissue strain around cell lacunae (Madi et al., 2020; Davis et al., 2025), the strains within individual trabeculae (Turunen et al., 2020), and in the entire trabecular network (Bonithon et al., 2021; Gillard et al., 2014), up to the whole-bone scale (Palanca et al., 2016). Furthermore, the accuracy of DVC has been assessed in numerous validation studies (Tozzi and Dall'Ara, 2025; Dall'Ara et al., 2017; Dall'Ara et al., 2014; Liu and Morgan, 2007). This technique has also been employed to investigate strain transfer within the joint, particularly focusing on diseased conditions (Madi et al., 2020; Ryan et al., 2020). For instance, the combination of high-resolution synchrotron nano-CT and DVC enabled the quantification of nanoscale strain in mineralized cartilage and subchondral bone of murine knee joints (Madi et al., 2020), highlighting mechanical response differences, in terms of strain patterns and fracture locations, between healthy and OA-predisposed knees. Micro-FE models have also been widely used to advance the understanding of bone and joint mechanics, particularly in the context of OA, osteoporosis, and mechanical adaptation (He et al., 2020; Oliviero et al., 2021; Zanjani-Pour et al., 2020).

While OA-related mechanical changes have been explored, the effect of aging on the epiphyseal strain distribution remains poorly characterized; yet, it is important to determine this effect, possibly without the influence of OA, on the mechanical response of the joint. Building on our previous results on microstructural and material modifications at the epiphysis in aged rats (Müller et al., 2026), this study aims to quantify and compare the mechanical environment within the epiphysis during aging using in situ knee compression, micro-CT imaging, DVC analysis, and micro-FE.

2. Materials and methods

2.1. Sample collection and preparation

Whole right legs were collected from adult (n = 6, 2-3 months old, mean body weight 447 g) and aged (n = 6, 13-15 months old, mean body weight 531 g) male Wistar rats immediately after animal sacrifice (body weight and age of individual animals are presented in the Supplementary Information, Table S1). Animals were obtained through an organ donation program at the Liège University Hospital (CHU), conducted under the approval of the Animal Ethics Committee of the University of Liège (IACUC-22-2416). Following harvesting, all samples were wrapped in gauze soaked with phosphate-buffered saline (PBS) and stored at −20 °C until testing. Prior to mechanical testing, each leg underwent a similar preparation protocol to ensure consistent knee positioning and to prevent joint dislocation during loading. One sample was processed and tested per day to avoid repeating freeze–thaw cycles. On the testing day, the leg was defrosted in a 37° water bath for 1 h. The foot and the soft tissues surrounding the femur and tibia were carefully removed with a scalpel, taking care to preserve the periarticular tissues of the knee. The tibia was manually aligned with its long axis oriented vertically, and its distal portion was embedded in a fast-hardening resin (Technovit 4071, Kulzer, Germany) until the tibial tuberosity. The vertically aligned and embedded tibia was then trimmed using a diamond saw (IsoMet Low Speed, Buehler, Germany) to fit into a custom-made loading device. This first embedding step ensured consistent tibial alignment across specimens and facilitated sample trimming. Positioning into the loading device was ensured using 3D-printed (Connex 260, Stratasys, USA) hexagonal cups, which restricted unwanted relative rotation between the femur and tibia during mechanical testing. Each specimen was placed into the loading device and glued to the cups at both tibial and femoral sides using the same fast hardening resin (Fig. 1A and B, and Supplementary Information, Fig. S1). During knee positioning in the loading device, a consistent knee angle position was ensured across specimens. To avoid dehydration during testing, the leg was wrapped in PBS-soaked gauze.

2.2. In situ mechanical testing and microcomputed tomography

The main focus of the mechanical testing was the tibial proximal epiphysis, which was directly loaded through the femur and the knee joint. A custom-made loading device previously used for testing the tibia and knee joints of mice was used to apply stepwise mechanical loading within a micro-CT scanner (VivaCT80, Scanco Medical, Bruettisellen, Switzerland) (Giorgi and Dall'Ara, 2018). Axial compression was applied manually using a screw–ball joint mechanism, and the magnitude of the axial load (aligned with the tibia axis) was monitored with a 100 N load cell (C9C, HBM, Germany). Images were acquired at each loading step with the micro-CT at a nominal isotropic voxel size of 10.4 μm. Following a previous protocol (Giorgi and Dall'Ara, 2018; Oliviero et al., 2018), the scanner operated at 55 keV voltage and 145 μA current intensity. With an integration time of 200 ms, combined with 750 projections and no frame averaging, each scan took approximately 30 min. To minimize beam hardening artifacts, a 0.5 mm-thick aluminum filter was used. Both geometry and densitometric calibration

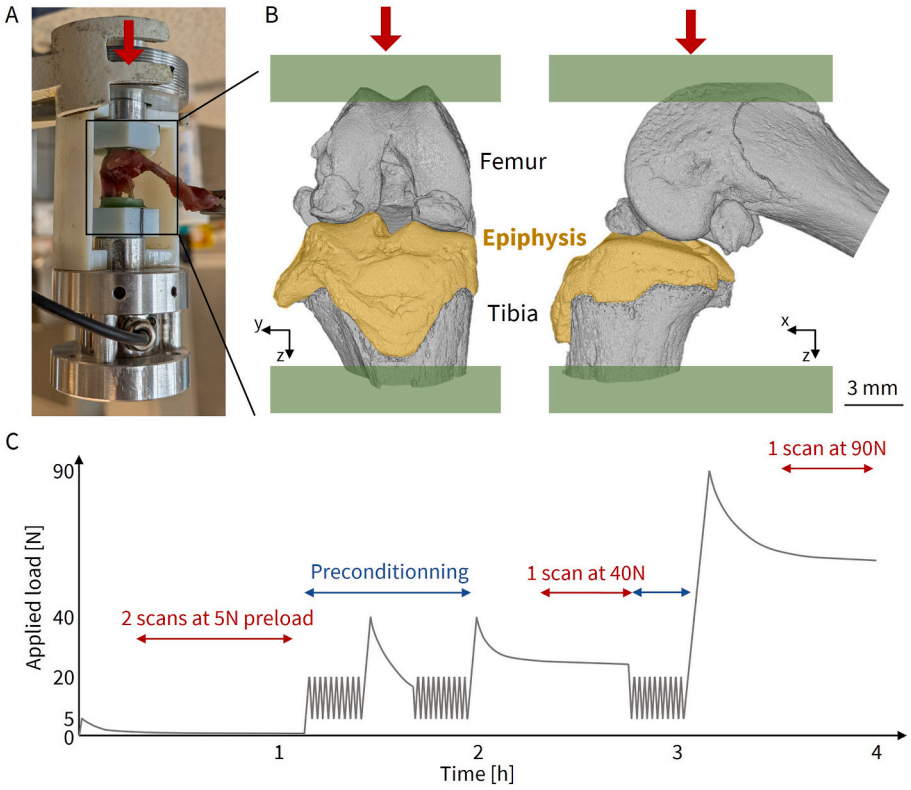

Fig. 1. Experimental setup and loading protocol. (A) Photograph of the loading device accommodating 3D-printed cups (white objects) and the tibia-knee-femur complex. (B) Schematic representation (based on micro-CT data) of the positioning of the femur and tibia within the resin (green blocks). The proximal part of the tibia, i.e. the epiphysis (highlighted in dark yellow) is the focus of our test. The resin-embedded bones are fixed to the custom 3D-printed cups placed inside the loading device. The red arrow indicates the loading direction. (C) Illustration of the loading protocol consisting of a preload, preconditioning cycles, two main loading steps at 40 N and 90 N, and waiting time for stressrelaxation. (For interpretation of the references to colour in this figure legend, the reader is referred to the Web version of this article.)

of the micro-CT were performed prior to the scans with a hydroxyapatite phantom and an aluminum rod of known volume and density.

Micro-CT scanning was combined with the following in situ loading protocol for the DVC analysis (Fig. 1C): after the application of a 5 N preload, two consecutive scans were acquired (preload scans); the load was then increased to 40 N, and another scan was performed; in a subsequent step, the load reached 90 N, and a final scan was done. The loading protocol was developed based on previous literature and following preliminary testing (unpublished data): the 40 N load was selected based on previous studies on rat tibia to elicit strains measurable with DVC (Gao et al., 2019; Liu et al., 2022). The higher load (90 N) was then applied to investigate possible strain localization phenomena under a traumatic loading event. At the same time, the higher load allowed to amplify the displacement and enhance DVC-strain estimation. After reaching the imposed load at each step (i.e., 5 N, 40 N, or 90 N), the loading plate was kept in position for 25-min to minimize the effect of stress relaxation and related movement artifacts. In addition, a preconditioning procedure was performed prior to the 40 N and 90 N loading steps to minimize the impact of soft tissues at the knee joint. The preconditioning consisted of ten cycles with maximum and minimum loads of 20 N and 5 N, respectively. Preliminary testing (unpublished data) indicated that two preconditioning cycles, separated by loading up to 40 N, were required before the main 40 N loading step to minimize the difference between the imposed load and the relaxation load.

2.3. Image processing and digital volume correlation (DVC)

Four scans were acquired and reconstructed for each specimen: two preload scans corresponding to the undeformed configuration and one scan per loading step. After virtually removing the distal portion of the femur, the sesamoid bones, and the mineralized portion of the meniscus, the micro-CT images at 40 N and 90 N were aligned with the corresponding preload scans using rigid registration, following a previous protocol with the software Amira (Amira 6.0.0, FEI Visualization Sciences Group, France; Normalized Mutual Information) (Oliviero et al., 2022). Being interested in the epiphysis and to minimize the impact of the potential deformation of the growth plate, the rigid registration was performed on the most distal portion of the proximal subchondral tibia. Specifically, a region of 30 voxels (or 312 μm) immediately above the growth plate was segmented and used for the registration. The resulting transformation matrix was then applied to the full scan, which was resampled using the Lanczos interpolator.

BoneDVC (Dall'Ara et al., 2017; Dall'Ara et al., 2014; Upload) was used to evaluate the internal displacements and strains within the epiphysis from the greyscale micro-CT images, excluding surrounding soft tissues (i.e., growth plate cartilage and articular cartilage). Briefly, after choosing a proper nodal spacing (see next section), a grid with the selected spacing was superimposed on the two input images (preloaded and deformed). The displacements at the nodes were then computed using a deformable registration toolkit (Sheffield Image Registration Toolkit, ShIRT), which solves globally the registration equations at the nodes of the grid assuming trilinear interpolation within each cell (Dall'Ara et al., 2017; Dall'Ara et al., 2014). The resulting displacement grid was then imported into a finite element software package (Ansys, V 15.0, Canonsburg, PA, USA), where grid nodes were converted into 8-node hexahedral elements, and the computed displacement fields were differentiated into strain fields. An algorithm implemented in the DVC workflow was used to remove all the nodes located outside the epiphysis, identified by a binary mask generated with the software CTAn (v1.19.4.0, Bruker). The components of the displacement (u_x, u_y, u_z) and

strain ($\varepsilon_x, \varepsilon_y, \varepsilon_z, \varepsilon_{xy}, \varepsilon_{xz}, \varepsilon_{yz}$) fields, as well as the maximum (ε_{Max}) and minimum (ε_{Min}) principal strains were calculated in each node.

2.4. DVC uncertainty analysis

A preliminary DVC uncertainty analysis was performed on two adult and two aged samples to determine the optimal nodal spacing (NS) for strain measurement and to evaluate the corresponding precision error. Broadly speaking, a low NS allows for a better spatial resolution but comes with higher errors in strain quantification (Dall'Ara et al., 2017; Dall'Ara et al., 2014). BoneDVC analyses were performed on the rigidly registered two repeated preload scans, using NS ranging from 55 to 75 voxels, in steps of 5 voxels. For each NS, the precision of strain measurement was quantified at each node using the standard deviation of the error (SDER), which is calculated as the standard deviation of the average of the absolute values of the six components of the strain tensor (Fig. 2) (Palanca et al., 2016; Liu and Morgan, 2007). A NS of 65 voxels provided the best compromise between measurement precision (113.29 ± 28.54 μstrain) and spatial resolution (676 μm).

2.5. Image-based microstructural finite element analysis

Image-based microstructural finite element (micro-FE) simulations were used to complement the DVC analysis. The models are based on micro-CT data acquired in a previous study considering 3 adult and 3 aged Wistar rats (of similar age to the animals used for DVC analyses) (Müller et al., 2026). At the time of sacrifice, animals had a mean body weight of 457 g (adult) and 687 g (aged). Briefly, the tibiae were scanned (Skyscan 1272, Bruker) freestanding rather than in the loading device, and a longer scanning time was imposed to allow for a higher signal-to-noise ratio. Other scanning parameters include a voltage of 90 kV, a current of 110 μA, an exposure time of 2300 ms, a frame averaging of 4, and a nominal isotropic voxel size of 10 μm. A 0.5 mm-thick aluminum and a 0.038 mm-thick copper filter were used to minimize beam hardening artifacts. After scanning, a three-dimensional Gaussian filter (square kernel size of 1.2) was applied, followed by binarization using a global thresholding approach based on the Otsu method (Otsu, 1979). The method analyzes the grey level histogram and searches for a threshold that maximizes inter-class variance, i.e., the separation between bone and background. After Gaussian filtering and thresholding, the binarized proximal tibiae were aligned vertically and then used as input for a custom MATLAB (MathWorks, USA) script to assign location-specific boundary conditions. Two ellipsoidal-shaped regions were identified on the proximal tibial surface at the level of the medial and lateral plateau, representing the contact areas with the femoral condyles (Lin et al., 2021; Wang et al., 2021). The semi-minor axes were set to 150 and 98 μm for the lateral and the medial plateau,

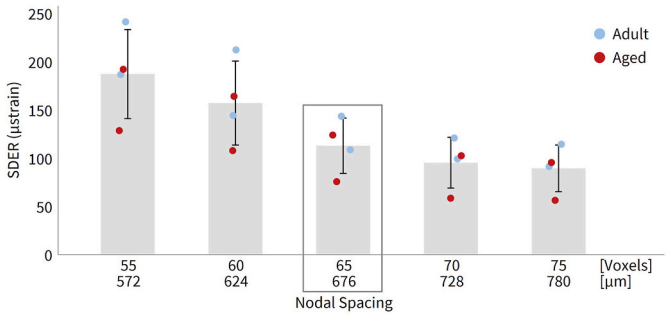

Fig. 2. DVC strain uncertainties evaluated as the standard deviation of the error (SDER), computed by comparing two repetitive scans of the same sample under a preload condition (5 N). A nodal spacing of 65 voxels is selected, leading to a mean SDER of 113.29 ± 28.54 μstrain. Bar plots represent the SDER mean value, error bars indicate one standard deviation, and individual samples are reported as scattered points.

respectively, while the semi-major axes were fixed at 175 and 112 μm. These geometric parameters were kept constant across all specimens, corresponding to a total surface for load application of about 82×10^3 μm^2 for the lateral and 34×10^3 μm^2 for the medial side. The position of the ellipse was slightly adjusted to match the morphology of each tibia. A vertical compressive force of 40 N was applied, equally distributed over the two ellipsoidal-shaped regions, while the distal surface was fully constrained (Fig. 6). As the micro-FE models also included the growth plate, which was either fully cartilaginous (adult rats) or presented mineralized bridges (aged rats), a soft layer mimicking growth plate cartilage (not visible in the micro-CT scans) was introduced to allow load transfer and convergence of the micro-FE simulations. The region located between the epiphysis and metaphysis, corresponding to growth plate cartilage, was described with homogeneous and isotropic material properties, with a Young's modulus of 50 MPa. Similarly, bone was also simplified as homogeneous and isotropic, with a Young's modulus of 25 GPa, derived from nanoindentation data (Müller et al., 2026) and consistent with previously reported values on rats measured in dehydrated conditions (Shipov et al., 2013). A Poisson ratio of 0.3 was assigned to both tissues. These material parameters were identical in both groups, which differed only in their microarchitecture. Micro-FE models were solved using ParOSol, an open-source voxel-based micro-FE linear elastic solver (Flaig et al., 2012), enabling efficient large-scale computation through parallel processing. All voxels were converted into hexahedral finite elements with trilinear shape functions, resulting in a total of approximately 85 and 91 million elements and 94 and 98 million nodes per sample for the adult and aged bones, respectively. Each model was solved on a NIC5 High Performance Computing cluster (CECI, ULiege) using 36 CPUs in about 6 h/sample. Micro-FE simulations were processed in MATLAB and Paraview (Ahrens et al., 2005) to obtain the apparent stiffness of the tibiae, computed as the ratio between the applied compressive load and the resulting nodal displacements, as well as the spatial distribution of the von Mises stresses and the effective strain (EFF) as defined in (Pistoia et al., 2002). Although von Mises stress is typically associated with yielding in ductile materials (which was not the focus of our work), we use it here as a convenient scalar measure that combines the different components of the stress tensor. This allows us to identify highly stressed regions and provides mechanical information complementary to the effective strains.

2.6. Statistics

Strains and displacements are reported as mean values ± standard deviation across the two groups. Statistical analysis was performed in MATLAB. For independent comparisons between age groups, Student's t-test was used when normality (Shapiro–Wilk) and equal variances (F-test) were confirmed, and Mann-Whitney *U* test otherwise. Following a previously developed analysis (Rummler et al., 2024), we compared intra-individual versus inter-individual differences of the strains. Considering the frequency distributions of the strains, the intra-individual differences were assessed by the mean of the standard deviations of each distribution, and the inter-individual differences were evaluated as the standard deviation of the means of the distributions. We also assessed the correlation between strains computed at 40 N and 90 N using Spearman's rank correlation coefficient ρ, which is appropriate for non-normally distributed data. Significance levels were set at $\alpha = 0.05$.

3. Results

Analyses at both load levels consistently revealed pronounced age-related differences. Here we present results for the 90 N load step, as fairly similar trends were observed for the 40 N load step (details in the Supplementary Information).

3.1. DVC analysis: mean displacements and strains

In a first analysis, displacements and strains were averaged over the entire epiphysis for each sample and compared between age groups. Adult samples exhibited significantly higher displacements than aged samples. As presented in Fig. 3A, the displacement magnitude reached 9.59 ± 3.47 μm in adults compared to 3.20 ± 1.63 μm in aged samples, corresponding to a 67% reduction with age ($p < 0.005$). An interesting observation is that loading the tibia through axial knee compression generated in the epiphysis both local negative (causing shortening) and positive (causing elongation) strains, referred to as compressive and tensile strains, respectively. Specifically, ε_{Min} equals to −1141 ± 562 μstrain in aged rats (63% lower than adult rats, $p < 0.001$) and ε_{Max} equals to 445 ± 84 μstrain in aged rats (67% lower than adults, $p < 0.005$) (Fig. 3B). Similar trends were obtained under 40 N loading (Supplementary Information, Fig. S2). These findings indicate a substantial stiffening of the tibial epiphysis with age.

3.2. DVC analysis: frequency distribution of the strains

The age-related differences were then further examined by analyzing the frequency distribution (normalized to unit area) of the principal strains (Fig. 3C and D). Both in adult and aged animals, the frequency distributions of minimum and maximum principal strains had an asymmetric shape and showed a peak. These distributions were rather similar for all animals within the same age group (Supplementary Information, Fig. S3). Adult samples displayed consistently broader distributions with peaks located at higher strains than aged ones. Strain heterogeneity, quantified as the full width at half maximum (FWHM) of the peak, was 2171 ± 836 μstrain for ε_{Min} and 1628 ± 387 μstrain for ε_{Max} in adults, compared to 1091 ± 403 μstrain for ε_{Min} and 847 ± 322 μstrain for ε_{Max} in aged samples. Peaks were located at −2210 ± 151 μstrain (ε_{Min}) and 659 ± 482 μstrain (ε_{Max}) in adult and −724 ± 266 μstrain (ε_{Min}) and 327 ± 84 μstrain(ε_{Max}) in aged samples (Supplementary Information, Table S2). Given the large heterogeneity of the strain distributions, the inter-individual strain variability was always lower than the intra-individual strain variability, for both compressive and tensile strains (Table 1 and Supplementary Information, Table S3).

3.3. DVC analysis: spatial maps of compressive and tensile principal strains

To gain insights into the load transmission in the epiphysis, we considered the spatial strain maps. Fig. 4 shows two-dimensional maps

Table 1
Intra- and inter-individual variability of maximum and minimum principal strains for each age group at the 90 N load step. Intra-individual variability was assessed by the mean of standard deviations of each distribution, while the inter-individual variability corresponds to the standard deviation of the distribution of the means.

Group	Mechanical Parameter	Intra-variability mean (SD) [μstrain]	Inter-variability SD (mean) [μstrain]
Adult	Compressive strain,$\lvert \varepsilon_{Min} \rvert$	1602	586
	Tensile strain, ε_{Max}	1577	350
Aged	Compressive strain, $\lvert \varepsilon_{Min} \rvert$	667	562
	Tensile strain, ε_{Max}	477	84

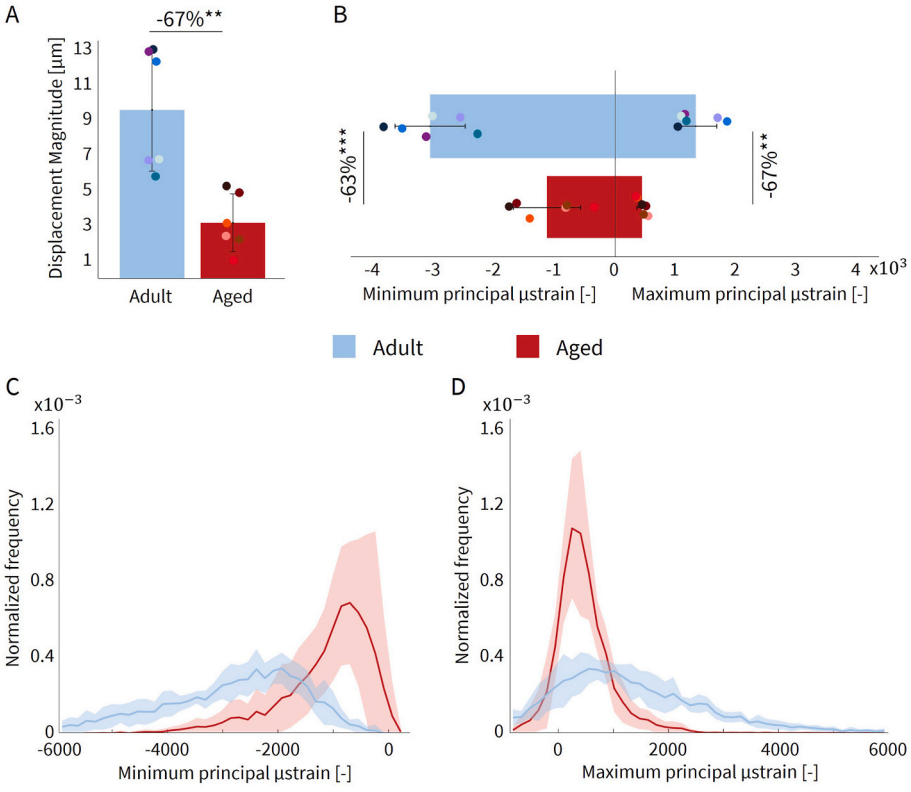

Fig. 3. DVC analysis of displacement and strain in the rat tibia epiphysis, following axial compression at 90 N. Comparison of (A) displacement magnitude, and (B) minimum and maximum principal strain between adult and aged samples. Histograms represent group means, with error bars indicating one standard deviation; individual samples are reported as scattered points. Statistical significance between the data sets is indicated as follows: *$p < 0.05$, **$p < 0.01$, ***$p < 0.001$, and ns (not significant). Frequency distributions of (C) minimum and (D) maximum principal strain within the epiphysis of adult (blue) and aged (red) samples. Solid lines represent the mean values across all specimens in each age group, and the shaded areas the standard deviation interval. (For interpretation of the references to colour in this figure legend, the reader is referred to the Web version of this article.)

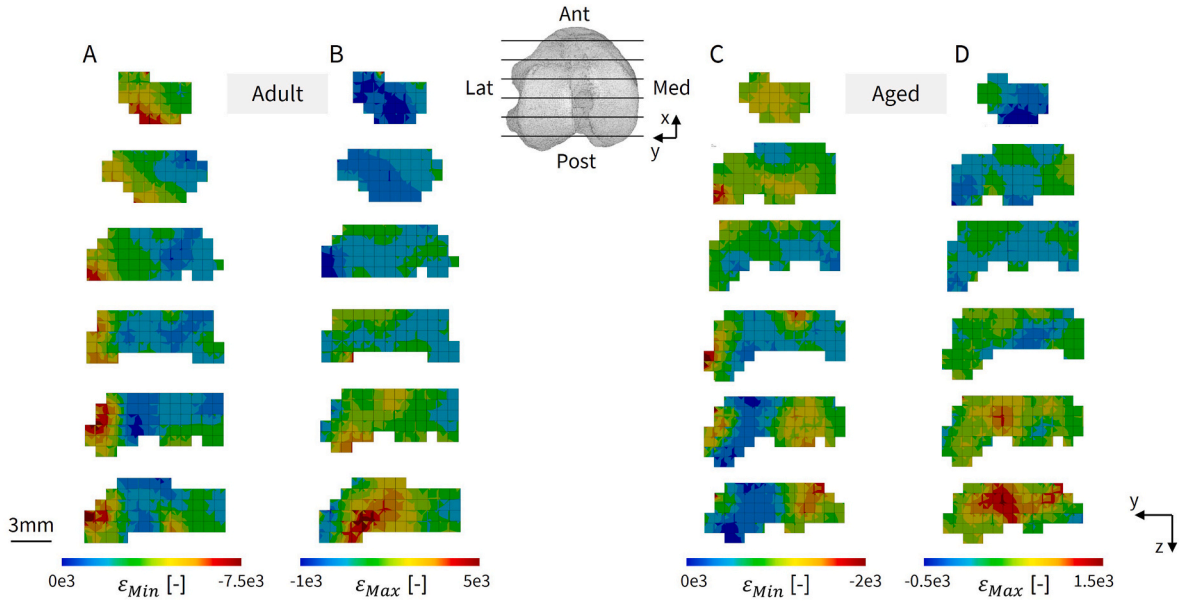

Fig. 4. Spatial maps of maximum and minimum principal strains in a representative (A, B) adult and (C, D) aged sample, following axial compression at 90 N. 2D maps are shown across several frontal sections of the epiphysis. Sections are displayed from anterior (top) to posterior (bottom).

of compressive and tensile principal strains considering multiple frontal sections for a representative adult (Fig. 4A and B) and aged (Fig. 4C and D) sample. In the adult sample, the highest compressive strains were located at the lateral border of the epiphysis. High strains were found at the posterior-medial side, while the central region showed relatively lower compressive deformations. High tensile strains were consistently concentrated in the posterior–lateral side and extended to the center of the epiphysis. In the aged animal, relatively higher compressive strains were also seen at the lateral border but also the medial side underwent higher compressive strains. Likewise, the region subjected to high tensile strains was the posterior one, but extending over a larger area than in adult bones. While all adult samples exhibited a fairly consistent behavior, the aged rats displayed a greater inter-individual variability with no clear general patterns discernible in the 2D maps (see also Supplementary Information, Fig. S4).

3.4. DVC analysis: comparison of strains at 40 N and 90 N

We compared the strains induced by different loadings (40 N and 90 N) in the same sample. In the scatter plots of Fig. 5, the strains measured at 40 N are plotted versus the strains measured at 90 N for each node in a representative adult and aged sample, distinguishing between minimum and maximum principal strains. In general, a moderate to strong correlation was observed between strains at 40 N and 90 N, indicating that regions highly strained at 40 N tend to be also highly strained at 90 N. Spearman's rank correlation coefficients were 0.82 ± 0.12 for ε_{Min} and 0.82 ± 0.05 for ε_{Max} in adult samples, and 0.71 ± 0.24 for ε_{Min} and 0.67 ± 0.16 for ε_{Max} in aged samples. However, the increase in absolute principal strain between 40N and 90N was lower than the increase in applied load: most data points lie to the right of the reference line with slope 2.25, given by 90 N/40 N (see also Supplementary Information, Fig. S5). Moreover, only a very small fraction of elements were strained beyond ±7000 μstrain, which is used as a rough indicator of tissue yielding (Kopperdahl and Keaveny, 1998; Morgan and Keaveny, 2001; Bayraktar et al., 2004). Specifically, in adult samples loaded with 90 N, less than 3% of the elements showed a ε_{Min} below −7000 μstrain. In aged samples, this percentage was even lower and remained below 0.12%. This suggests that inelastic deformation remains

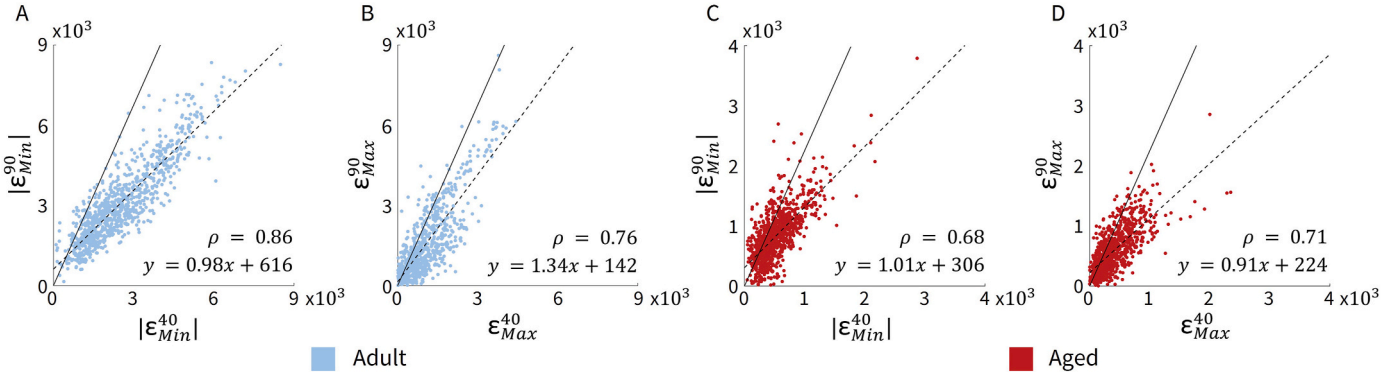

Fig. 5. Correlation between minimum (A, C) or maximum (B, D) principal strains calculated in the subchondral tibia when the knee joint is loaded with different load magnitudes (90 N on y-axis, 40 N on x-axis). Results are reported for a representative adult (blue) and aged (red) sample. Each point represents the same location evaluated at the two different loads. The solid line with a slope of 2.25 (=90 N/40 N) is added to estimate the increase in strain with respect to the increase in applied load. The dotted line indicates a linear regression between the two loadings (with the corresponding parameters reported in the plots). The relationship between strains is quantified using Spearman's correlation coefficient ρ, reported in the plots. (For interpretation of the references to colour in this figure legend, the reader is referred to the Web version of this article.)

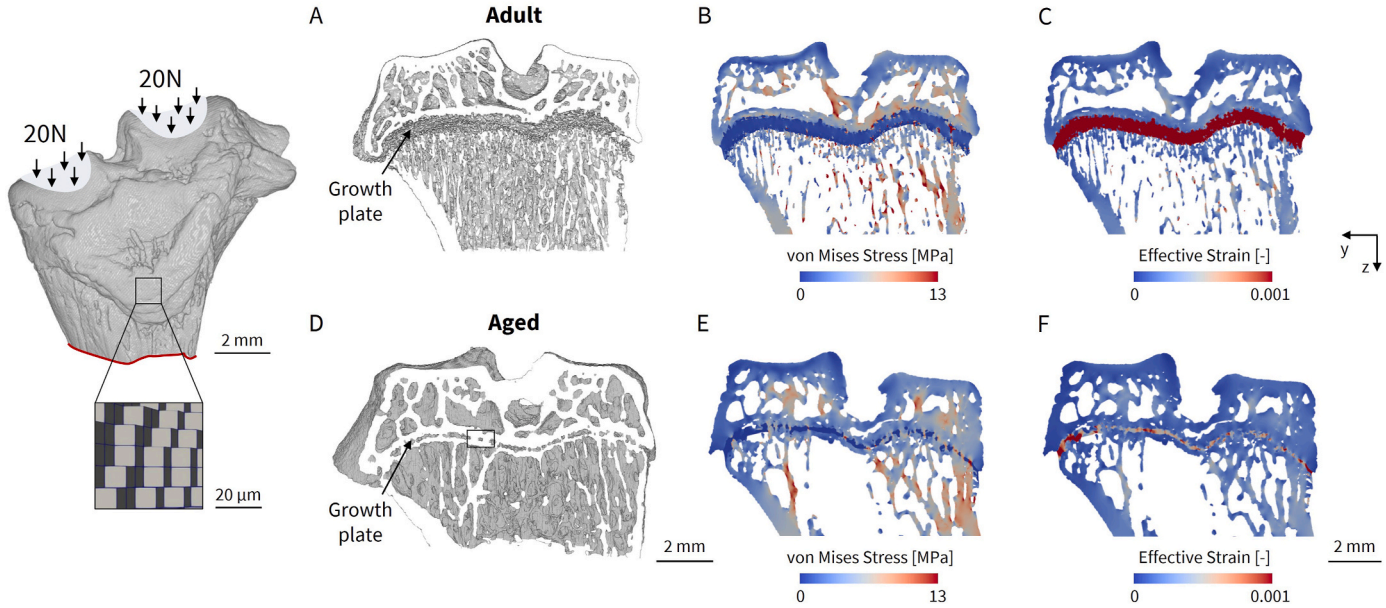

Fig. 6. Image-based micro-structural finite element (micro-FE) modeling and results on load transfer. (Left) Representative proximal tibia with two ellipsoidal-shaped regions (in light cyan) highlighting the location of load application (vertical compressive force of 20 N on each side). The bottom surface (shown in red) was fully constrained. The inset illustrates the hexahedral mesh elements. (Right) Representative frontal section of micro-CT images showing epiphysis and metaphysis separated by the growth plate in (A) adult and (B) aged samples. While in adult samples the growth plate region is mainly cartilaginous, in aged samples several mineralized bridges are visible (one large bridging region is highlighted by the black rectangle). von Mises stress (B, E) and effective strain (C, F) maps computed with micro-FE, highlighting the load transfer through the bridges in aged samples (E) and the large deformation of the growth plate in adult ones (C). (For interpretation of the references to colour in this figure legend, the reader is referred to the Web version of this article.)

very limited, even under 90 N loading, which is much higher than assumed physiological loading.

3.5. Micro-FE analysis: apparent stiffness and load transfer across the growth plate

Micro-FE simulations highlighted a substantial increase in apparent stiffness of the proximal tibia with aging: adult samples had a stiffness of 4415 ± 456 N/mm compared to 25882 ± 4983 N/mm measured in aged ones. In adult samples, relatively low stresses but high strains were observed at the growth plate, this region being mainly cartilaginous (Fig. 6A–C). Conversely, in aged samples, mineralized bridges connecting the epiphysis with the metaphysis appeared: those locations carried high stresses and helped to reduce the overall strain at the growth plate (Fig. 6D–F), thereby contributing to increasing the apparent stiffness. These mechanical features are well in line with microstructural variations: with aging, we found a decrease in growth-plate thickness of about 45% and a large increase in the volume fraction of mineralized bridges of almost 110% on a subset of animals belonging to the same strain and age groups (Supplementary Information, Note 1 and Fig. S6).

4. Discussions

This study aimed at investigating the effect of aging on the full-field internal strains within the rat tibial epiphysis, a region particularly important for load transmission across the knee joint (Malekipour et al., 2013; Stewart and Kawcak, 2018). Three-dimensional displacements and strains under loading were measured by combining in situ axial knee compression with micro-CT imaging and global DVC analysis. Such results were also complemented by micro-FE analysis. Our main finding is that aging leads to significantly reduced strains in the tibia epiphysis, leading to a substantial apparent stiffening of that region as indicated by micro-FE simulations. In aged animals, the strain field was not simply "uniformly rescaled", but we observed less heterogeneous strain distributions, distinct 3D spatial strain patterns, and increased inter-sample variability.

Several studies have reported age-related architectural changes in the epiphysis, which are specific to the animal model and age group considered (Ren et al., 2018; Ries et al., 2020; Goliath et al., 2022). In a previous work, analyzing animals of the same strain and age, we found that, at the microstructural level, aging leads to a marked thickening of the subchondral bone plate together with coarsening of the subchondral trabecular bone with fewer, thicker, and more spaced trabeculae. At the material level, subchondral bone was more mineralized and displayed an increased indentation modulus (Müller et al., 2026). Together, these structural and material changes provide a conceivable cause for the lower strains observed in aged samples. This is consistent with another study on murine cortical and trabecular bone, reporting lower strains with aging, primarily due to morphological changes, with variations in tissue material properties playing a secondary role (Razi et al., 2015). In the context of bone mechanical adaptation, aged rats typically have greater body weight, and consequently, their bones are exposed to higher mechanical loads. According to Frost's mechanostat hypothesis (Frost, 2003), increased loading should enhance mechanical stimulation and promote greater bone mass. However, with aging, bone mechanosensitivity may decline. When reduced mechanoresponsiveness is combined with the lower strain observed in aged samples, the overall mechanical adaptation of bone may become compromised. This could represent a biological factor underlying the substantial stiffening of the epiphysis in aged rats. As the epiphysis is believed to have a mechanical protective function for articular cartilage by facilitating load distribution and impact attenuation (Malekipour et al., 2013; Stewart and Kawcak, 2018), a stiffer epiphysis may alter cartilage loading and contribute to increasing the likelihood of joint degeneration.

The reduced heterogeneity in strain frequency distributions under aged conditions may be partially attributable to trabecular coarsening. Considering that trabecular bone is bending-dominated (Gibson, 2005), each trabecula should carry both relatively low strains, close to the neutral axis, and higher strains far from it, resulting in a highly

heterogeneous strain pattern (Zwahlen et al., 2015). A sparse trabecular network with fewer and thicker trabeculae may limit the overall degree of strain heterogeneity. While all adult specimens exhibited relatively consistent spatial strain patterns, suggesting a comparable loading application across the samples, aged rats showed a higher inter-sample variability. With fewer and thicker trabeculae, load transfer may become more sensitive to the orientation and connectivity of individual trabeculae, leading to high inter-sample variability depending on the sample-specific trabecular arrangement. However, while it is well-known that apparent-level mechanical properties of trabecular bone (i.e., stiffness and strength) are strongly correlated with bone volume fraction and trabecular architecture (Zysset, 2003; Maquer et al., 2015; Bregoli et al., 2024; Zysset et al., 2013), as indicated by many works based on microstructural finite element modeling, the relationship between microstructural parameters and DVC-derived strains is less established, especially at the level of individual trabeculae. A study applying stepwise compression to whole human femoral heads found that trabecular thickness and connectivity density (globally assessed) were strongly associated with strains, and trabecular thickness was also an indicator of the percentage of bone tissue exceeding the yield strain (Ryan et al., 2020). A characterization of the interplay between microstructural parameters and mechanical strains, performed considering whole human vertebrae, revealed a complex strain–microstructure relationship, whereby the microstructural parameters most strongly correlated with strain varied across spatial locations within the vertebra (Tanoto et al., 2024).

The methodology employed in this study enabled quantitative assessment of epiphyseal strains while keeping the knee joint as intact as possible and in close-to-native conditions. The measured mean principal strains with the considered spatial resolution of a few hundred micrometers were consistently above the DVC error. Specifically, for the lower load step (40 N) and in aged rats (which showed the lowest deformation), the average tensile and compressive strains were 3.2 and 7.3 times greater than the mean error, respectively. The reliability of our approach is further supported by the strong correlation between strains measured at 40 N and 90 N, despite load removal and sample repositioning into the micro-CT between the loading steps. Moreover, even though in adult rats the epiphysis is connected to the metaphysis through a relatively compliant cartilaginous growth plate (Fischenich et al., 2022; Eckstein et al., 2022), by registering the scans above this region, we could measure the mechanical behavior independent of the large displacement happening at the growth plate. The epiphysis experiences heterogeneous deformation, including both compressive and tensile strains. This finding arises from the complex multi-tissue load transmission at the knee, combined with the interplay between cortical and trabecular compartments and overall epiphyseal morphology. The subchondral plate may experience some bending when loaded by the femoral condyle. As individual trabeculae tend to deform in bending (Gibson, 1985, 2005), both compressive and tensile strains are generated. The strain patterns appear to be influenced also by the relative tibiofemoral alignment and bone contact locations during loading. In particular, the tibiofemoral joint contact on the medial plateau occurs in the posterior region, whereas on the lateral plateau, it is in a more central location (Supplementary Information, Fig. S7). The high tensile strains concentrated in the postero-lateral region could reflect a bending of the plateau under central compression. In contrast, the posterior medial plateau undergoes predominantly compressive strains, consistent with the contact position of the femoral condyle on the medial plateau. This contact configuration, resulting from the experimental protocol, is consistently observed in all samples, except for two aged samples, where some variations in the contact regions were present.

Although in this work we primarily focused on the epiphysis, a comprehensive understanding of the load transmission across the joint should also consider the growth plate. As previously mentioned, in rats, the growth plate does not fully fuse and remains cartilaginous; yet, it shows age-related thinning (Roach et al., 2003; Forcinito et al., 2011) and progressive formation of mineralized bridges connecting the epiphysis to the metaphysis (Roach et al., 2003). Those changes were apparent in the micro-CT images acquired in the present study (Fig. 6). Growth-plate thinning and mineralized bridges reduced growth-plate compliance; combined with limited epiphyseal deformation, this may increase the mechanical burden on articular cartilage in aging conditions.

This study has some limitations that should be mentioned. Firstly, the loading protocol does not fully reproduce physiological loading conditions in the rat. Sample fixation and loading direction were chosen to ensure stable and repeatable loading across the samples. Specifically, a knee flexion angle of about 60° was selected and kept constant, based on experimental feasibility rather than on physiological joint posture. Angles closer to full extension (0°) would cause the femur to slide on the tibial plateau upon loading. Higher flexion angles would increase the effective size of the system, requiring a larger sample-to-detector-distance and, consequently, a lower resolution and increased imaging artifacts. We used two peak loads (40 N and 90 N), which, even after stress relaxation (decreasing to approximately 25 N and 65 N, respectively), were much higher than assumed physiological loading. Hindlimb forces in rodents during strenuous activities are about twice the body weight (Roach et al., 2012). Even if we assumed a fixed strain threshold as an indicator of tissue yield, without distinguishing between the different mineralized tissues at the subchondral region (i.e., the cortical plate, the trabecular bone, and the mineralized cartilage), we observed only a very small fraction of elements strained above the assumed yield. Especially for the aged rats, even decreasing the threshold should not lead to large failure regions under 90 N loading. When comparing mean strain and frequency distributions of adult and aged samples across the two loading conditions, a qualitatively similar trend was observed. In general, regions exhibiting high strain remained fairly consistent between 40 N and 90 N loads, suggesting that prevalent deformation modes observed at 90 N are representative of those occurring at the lower load step. Moreover, strains measured at the same location under 40 N and 90 N showed moderate to strong correlations, consistent with a largely preserved spatial pattern of deformation. Interestingly, strains at 90 N increased less than expected from the increase in applied load. This may reflect load redistribution phenomena among different joint tissues (i.e., femur and tibia, as well as meniscus, growth plate, and metaphysis), which may “release” the strain in the epiphysis such that the effective load reaching the epiphysis may be lower than the external load applied at the knee.

A second limitation concerns the spatial resolution of the DVC analysis, which does not allow a detailed investigation of trabecular and cortical contributions to load transfer. As a result, a direct correlation between the location of high strain and structural features remains challenging. Clearly, we also could not measure strains within individual trabeculae, which usually requires very high resolution and fast imaging methods (Roach et al., 2012), as offered, for example, by synchrotron facilities, but coming with the additional cost of radiation damage and a small field of view (Peña Fernández et al., 2018; Dall’Ara et al., 2022). Even with knowledge of strain at the individual trabecular level, it remains unanswered whether morphological analysis of the trabecular structure can predict local regions subjected to high strain. Given the complex three-dimensional architecture of trabecular bone, there is no guarantee that thin trabeculae will experience the highest strain, as indicated by studies on cellular structures (Ruffoni et al., 2010; Maurer et al., 2015).

Thirdly, we did not attempt to image articular cartilage. The main reason is that we prioritized in situ compression of the entire epiphysis with a clear limitation on the achievable resolution. Following our finding of a substantial stiffening of the epiphysis with aging, the next obvious question is about the impact of such mechanical modification on articular cartilage deformation. Previous works focusing on OA suggested that when subchondral bone loses its capacity to distribute and dissipate loads, cartilage may experience higher and more localized

stresses, promoting degeneration (Hu et al., 2021; Donell, 2019). Contrast agents allow to visualize cartilage with micro-CT (Disney et al., 2017; Clark et al., 2020; Descamps et al., 2014), but affect the mechanical behavior of this tissue (Davis et al., 2024). Considering that cartilage thickness in rat tibiae is approximately 0.5 mm (Xie et al., 2009; Roemhildt et al., 2006), with our settings (resolution and field of view), contrast-enhanced micro-CT would have allowed us to measure only thickness variations but not tissue strains.

Fourthly, differences between rats and humans in growth plate (Ağırdil, 2020; Haimov et al., 2020), bone architecture (Barak et al., 2013), and tissue material properties (Shipov et al., 2013; Tits et al., 2023) limit direct quantitative translation of our results to the medical setting. However, the laboratory rat is one of the most widely used animal models in pre-clinical research, and, in this context, it is of high importance to characterize knee joint mechanics in aging. Even if the Wistar rats usually do not show spontaneous OA, it allowed us to characterize age-related changes independent of the outburst of the disease. Future studies could investigate whether similar changes are observed in a post-traumatic context, for instance, using a destabilization of the medial meniscus (DMM) model adapted for rats (Rajalekshmi and Agrawal, 2025).

Finally, the microstructural analyses were not performed on the specimens used for the DVC experiments, as these measurements were conducted in a previous study on tibiae from rats of the same strain and age, considering 10 samples per group. Given the low variability of laboratory rodents, we assumed that the specimens used in this study exhibit comparable microarchitectural properties. For image quality reasons, the micro-FE analyses were also performed on the scans from the previous study; therefore, a direct quantitative comparison between the micro-FE and DVC results is not possible. Nevertheless, several previous studies have conducted such comparisons and generally reported good agreement (Costa et al., 2017; Oliviero et al., 2018; Cech and Tink, 2023). In our work, micro-FE was used to extract complementary information not available with DVC. In these micro-FE simulations, the growth plate cartilage layer was modeled as a linear elastic material with a Young's modulus of 50 MPa due to restrictions in the micro-FE solver, although growth plate cartilage exhibits poroelastic time-dependent behavior. This modulus value is higher than values typically found in literature (Eckstein et al., 2022). Indeed, reported values vary widely depending on measuring techniques, testing conditions, strain rate, loading direction, and specific zones, with elastic modulus typically ranging from 0.1 to 10 MPa (Eckstein et al., 2022; Radhakrishnan et al., 2004; Sergerie et al., 2009; Villemure and Stokes, 2009; Cohen et al., 1998). This assumption has a limited impact on this study as the major focus is on the strain in the bone tissue, rather than in the growth plate. Additionally, for adult rats, where the growth plate is fully cartilaginous, the apparent stiffness becomes highly dependent on the cartilage elastic modulus. The high value chosen here takes somewhat into account the stiffening of cartilage under dynamic loading and in confined conditions ("squeezed" between two bone compartments). Using lower values would even increase the differences in apparent stiffness with aging. Furthermore, bone was described with a homogeneous Young's modulus, even if a heterogeneous distribution of tissue modulus can offer a more realistic representation of bone's mechanical behavior (Marcián et al., 2021). However, using a heterogeneous modulus may introduce additional uncertainties related to the conversion from grey level to tissue mineral density (which is particularly challenging due to beam hardening) (Kazakia et al., 2008), as well as to the identification of suitable density–elasticity relationships (which may be affected by tissue anisotropy and aging) (Tits et al., 2023; Granke et al., 2013; Akkus et al., 2004; Turunen et al., 2012). Being mainly interested in the apparent stiffness as well as in the impact of growth plate specificities on the load transfer from epiphysis to metaphysis, we opted for a more straightforward approach based on a homogeneous tissue modulus.

In conclusion, we found that aging alters load transfer mechanisms across the rat knee joint, with bone beneath articular cartilage becoming less deformable and therefore stiffer. Our findings motivate future research evaluating the impact of those changes on articular cartilage, which, in aged conditions, may sustain a more challenging mechanical environment. From a mechanobiological point of view, it would also be interesting to evaluate mechanisms of mechanical adaptation at the knee joint to understand the interplay between subchondral bone remodeling and joint degeneration.

CRediT authorship contribution statement

Laura Müller: Conceptualization, Data curation, Formal analysis, Funding acquisition, Investigation, Methodology, Visualization, Writing – original draft. **Sriram Kunnoth:** Formal analysis, Investigation, Methodology, Software. **Hajar Souhail:** Formal analysis, Investigation, Methodology, Software, Writing – original draft. **Margaux Ska:** Formal analysis, Methodology, Software. **Piyush Uniyal:** Formal analysis, Methodology, Software. **Luca D'Andrea:** Formal analysis, Investigation, Methodology, Software, Writing – original draft. **Pasquale Vena:** Formal analysis, Investigation, Methodology, Resources, Software, Writing – original draft. **G Harry van Lenthe:** Investigation, Methodology, Resources, Software. **Enrico Dall'Ara:** Conceptualization, Data curation, Funding acquisition, Investigation, Methodology, Project administration, Resources, Software, Supervision, Validation, Writing – original draft. **Davide Ruffoni:** Conceptualization, Data curation, Funding acquisition, Investigation, Methodology, Project administration, Resources, Software, Supervision, Validation, Writing – original draft.

Declaration of competing interest

The authors declare that they have no known competing financial interests or personal relationships that could have appeared to influence the work reported in this paper.

Acknowledgements

L.M. obtained funding from F.R.S.-FNRS as part of a FRIA grant (no. FC 47333) and further acknowledges the support of the Mobility Award of the European Society of Biomechanics (ESB), allowing a research stay at the University of Sheffield. This work was partially funded by the Excellence Science (EOS) program (EOS no. 40007553). H.S. is supported by the European Union's Horizon Europe program under the MSCA Doctoral Network (REBONE, grant agreement no. 101119884). We acknowledge the use of the high-performance computing resources of the CECI, funded by the F.R.S.-FNRS and the Walloon Region. Thierry Marchal from ANSYS Belgium is gratefully acknowledged for providing access to ANSYS through a partnership agreement. Quentin Grossman from the MBBM laboratory (ULiege) is acknowledged for printing the sample holders.

Appendix A. Supplementary data

Supplementary data to this article can be found online at https://doi.org/10.1016/j.jmbbm.2026.107481.

Data availability

Data will be made available on request.

References

Ahrens, J., Geveci, B., Law, C., 2005. ParaView: an end-user tool for large data visualization. Visualiz. Handbook.

Akkus, O., Adar, F., Schaffler, M.B., 2004. Age-related changes in physicochemical properties of mineral crystals are related to impaired mechanical function of cortical bone. Bone 34 (3), 443–453.

Ağırdil, Y., 2020. The growth plate: a physiologic overview. EFORT Open Rev. 5 (8), 498–507.
Barak, M.M., Lieberman, D.E., Hublin, J.-J., 2013. Of mice, rats and men: trabecular bone architecture in mammals scales to body mass with negative allometry. J. Struct. Biol. 183 (2), 123–131.
Bayraktar, H.H., Morgan, E.F., Niebur, G.L., et al., 2004. Comparison of the elastic and yield properties of human femoral trabecular and cortical bone tissue. J. Biomech. 37 (1), 27–35.
Bonithon, R., Kao, A.P., Fernández, M.P., et al., 2021. Multi-scale mechanical and morphological characterisation of sintered porous magnesium-based scaffolds for bone regeneration in critical-sized defects. Acta Biomater. 127, 338–352.
Bregoli, C., Biffi, C.A., Tuissi, A., et al., 2024. Effect of trabecular architectures on the mechanical response in osteoporotic and healthy human bone. Med. Biol. Eng. Comput. 62 (11), 3263–3281.
Cech, D.J., Tink, M.S., 2023. Functional Movement Development Across the Life Span [Internet]. Elsevier [cited 2026 Jan 2]. Available from: https://www.scribd.com/document/904487964/Functional-Movement-Development-Across-the-Life-Span-Third-Edition-Donna-J-Cech-Ms-Pt-Pcs-Dhs-instant-download.
Clark, J.N., Garbout, A., Ferreira, S.A., et al., 2020. Propagation phase-contrast micro-computed tomography allows laboratory-based three-dimensional imaging of articular cartilage down to the cellular level. Osteoarthr. Cartil. 28 (1), 102–111.
Cohen, B., Lai, W.M., Mow, V.C., 1998. A transversely isotropic biphasic model for unconfined compression of growth plate and chondroepiphysis. J. Biomech. Eng. 120 (4), 491–496.
Costa, M.C., Tozzi, G., Cristofolini, L., et al., 2017. Micro Finite Element models of the vertebral body: validation of local displacement predictions. PLoS One 12 (7), e0180151.
Dall'Ara, E., Barber, D., Viceconti, M., 2014. About the inevitable compromise between spatial resolution and accuracy of strain measurement for bone tissue: a 3D zero-strain study. J. Biomech. 47 (12), 2956–2963.
Dall'Ara, E., Bodey, A.J., Isaksson, H., et al., 2022. A practical guide for *in situ* mechanical testing of musculoskeletal tissues using synchrotron tomography. J. Mech. Behav. Biomed. Mater. 133, 105297.
Dall'Ara, E., Peña-Fernández, M., Palanca, M., et al., 2017. Precision of digital volume correlation approaches for strain analysis in bone imaged with micro-computed tomography at different dimensional levels. Front. Mater. 4 [Internet][cited 2025 Nov 11].
Dall'Ara, E., Tozzi, G., 2022. Digital volume correlation for the characterization of musculoskeletal tissues: current challenges and future developments. Front. Bioeng. Biotechnol. 10, 1010056.
Davis, S., Karali, A., Balcaen, T., et al., 2024. Comparison of two contrast-enhancing staining agents for use in X-ray imaging and digital volume correlation measurements across the cartilage-bone interface. J. Mech. Behav. Biomed. Mater. 152, 106414.
Davis, S., Karali, K., Zekonyte, J., et al., 2025. 3D full-field strain distribution across the osteochondral unit during osteoarthritis progression. View 6 (6), 20250062.
Descamps, E., Sochacka, A., Kegel, B.D., et al., 2014. Soft tissue discrimination with contrast agents using micro-CT scanning. Belg. J. Zool. 144 (1) [Internet][cited 2026 Jan 20].
Disney, C.M., Madi, K., Bodey, A.J., et al., 2017. Visualising the 3D microstructure of stained and native intervertebral discs using X-ray microtomography. Sci. Rep. 7 (1), 16279.
Donell, S., 2019. Subchondral bone remodelling in osteoarthritis. EFORT Open Rev. 4 (6), 221–229.
Eckstein, K.N., Thomas, S.M., Scott, A.K., et al., 2022. The heterogeneous mechanical properties of adolescent growth plate cartilage: a study in rabbit. J. Mech. Behav. Biomed. Mater. 128, 105102.
Fischenich, K.M., Schneider, S.E., Neu, C.P., et al., 2022. Material properties and strain distribution patterns of bovine growth plate cartilage vary with anatomic location and depth. J. Biomech. 134, 111013.
Flaig, C., Arbenz, P., 2012. A highly scalable matrix-free multigrid solver for μFE analysis based on a pointer-less octree. In: Lirkov, I., Margenov, S., Waśniewski, J. (Eds.), Large-Scale Scientific Computing. Springer, Berlin, Heidelberg, pp. 498–506.
Forcinito, P., Andrade, A.C., Finkielstain, G.P., et al., 2011. Growth-inhibiting conditions slow growth plate senescence. J. Endocrinol. 208 (1), 59–67.
Frost, H.M., 2003. Bone's mechanostat: a 2003 update. Anat. Rec. A Discov. Mol. Cell Evol. Biol. 275 (2), 1081–1101.
Gao, J., Liu, B., Zhang, M., et al., 2019. Strain distribution evaluation of rat tibia under axial compressive load by combining strain gauge measurement and finite element analysis. Appl. Bionics Biomech. 2019, 1736763.
Gibson, L.J., 1985. The mechanical behaviour of cancellous bone. J. Biomech. 18 (5), 317–328.
Gibson, L.J., 2005. Biomechanics of cellular solids. J. Biomech. 38 (3), 377–399.
Gillard, F., Boardman, R., Mavrogordato, M., et al., 2014. The application of digital volume correlation (DVC) to study the microstructural behaviour of trabecular bone during compression. J. Mech. Behav. Biomed. Mater. 29, 480–499.
Giorgi, M., Dall'Ara, E., 2018. Variability in strain distribution in the mice tibia loading model: a preliminary study using digital volume correlation. Med. Eng. Phys. 62, 7–16.
Goliath, J.R., Gosman, J.H., Stout, S.D., et al., 2022. Ontogenetic patterning of human subchondral bone microarchitecture in the proximal tibia. Biology 11 (7), 1002.
Granke, M., Gourrier, A., Rupin, F., et al., 2013. Microfibril orientation dominates the microelastic properties of human bone tissue at the lamellar length scale. PLoS One 8 (3), e58043.
Gross, T., Pahr, D.H., Peyrin, F., et al., 2012. Mineral heterogeneity has a minor influence on the apparent elastic properties of human cancellous bone: a SRuCT-based finite element study. Comput. Methods Biomech. Biomed. Eng. 15 (11), 1137–1144.
Haimov, H., Shimoni, E., Brumfeld, V., et al., 2020. Mineralization pathways in the active murine epiphyseal growth plate. Bone 130, 115086.
He, Z., Chu, L., Liu, X., et al., 2020. Differences in subchondral trabecular bone microstructure and finite element analysis-based biomechanical properties between osteoporosis and osteoarthritis. J. Orthop. Transl. 24, 39–45.
Hu, Y., Chen, X., Wang, S., et al., 2021. Subchondral bone microenvironment in osteoarthritis and pain. Bone Res. 9 (1), 20.
Kazakia, G.J., Burghardt, A.J., Cheung, S., et al., 2008. Assessment of bone tissue mineralization by conventional x-ray microcomputed tomography: Comparison with synchrotron radiation microcomputed tomography and ash measurements. Med. Phys. 35 (7Part1), 3170–3179.
Kopperdahl, D.L., Keaveny, T.M., 1998. Yield strain behavior of trabecular bone. J. Biomech. 31 (7), 601–608.
Li, G., Zheng, Q., Landao-Bassonga, E., et al., 2015. Influence of age and gender on microarchitecture and bone remodeling in subchondral bone of the osteoarthritic femoral head. Bone 77, 91–97.
Lin, C.-C., Lu, H.-L., Lu, T.-W., et al., 2021. Reconstruction of three-dimensional tibiofemoral kinematics using single-plane fluoroscopy and a personalized kinematic model. Appl. Sci. 11 (20) [Internet][cited 2026 Jan 24].
Liu, Z., Gao, J., Gong, H., 2022. The adaptive response of rat tibia to different levels of peak strain and durations of experiment. Med. Eng. Phys. 102, 103785.
Liu, L., Morgan, E.F., 2007. Accuracy and precision of digital volume correlation in quantifying displacements and strains in trabecular bone. J. Biomech. 40 (15), 3516–3520.
Lotz, J.C., Gerhart, T.N., Hayes, W.C., 1991. Mechanical properties of metaphyseal bone in the proximal femur. J. Biomech. 24 (5), 317–329.
Lotz, M., Loeser, R.F., 2012. Effects of aging on articular cartilage homeostasis. Bone 51 (2), 241–248.
Madi, K., Staines, K.A., Bay, B.K., et al., 2020. In situ characterization of nanoscale strains in loaded whole joints via synchrotron X-ray tomography. Nat. Biomed. Eng. 4 (3), 343–354.
Malekipour, F., Whitton, C., Oetomo, D., et al., 2013. Shock absorbing ability of articular cartilage and subchondral bone under impact compression. J. Mech. Behav. Biomed. Mater. 26, 127–135.
Maquer, G., Musy, S.N., Wandel, J., et al., 2015. Bone volume fraction and fabric anisotropy are better determinants of trabecular bone stiffness than other morphological variables. J. Bone Miner. Res. 30 (6), 1000–1008.
Marcián, P., Borák, L., Zikmund, T., et al., 2021. On the limits of finite element models created from (micro)CT datasets and used in studies of bone-implant-related biomechanical problems. J. Mech. Behav. Biomed. Mater. 117, 104393.
Maurer, M.M., Weinkamer, R., Müller, R., et al., 2015. Does mechanical stimulation really protect the architecture of trabecular bone? A simulation study. Biomech. Model. Mechanobiol. 14 (4), 795–805.
Müller, L., Blouin, S., Pedrinazzi, E., et al., 2026. Aging modifies microstructure and material properties of mineralized cartilage and subchondral bone in the murine knee. bioRxiv [Internet][cited 2026 Apr 14]. p. 2026.04.02.716015. Available from: https://www.biorxiv.org/content/10.64898/2026.04.02.716015v1.
Morgan, E.F., Keaveny, T.M., 2001. Dependence of yield strain of human trabecular bone on anatomic site. J. Biomech. 34 (5), 569–577.
Namiranian, B., Doi, K., Alenezi, S., et al., 2025. Bone evaluation with micro finite element analysis in animal models. Tomography 11 (9), 101.
Oliviero, S., Cheong, V.S., Roberts, B.C., et al., 2022. Reproducibility of densitometric and biomechanical assessment of the mouse tibia from in vivo Micro-CT images. Front. Endocrinol. [Internet] [cited 2026 Jan 24];13.
Oliviero, S., Giorgi, M., Dall'Ara, E., 2018. Validation of finite element models of the mouse tibia using digital volume correlation. J. Mech. Behav. Biomed. Mater. 86, 172–184.
Oliviero, S., Roberts, M., Owen, R., et al., 2021. Non-invasive prediction of the mouse tibia mechanical properties from microCT images: comparison between different finite element models. Biomech. Model. Mechanobiol. 20 (3), 941–955.
Otsu, N., 1979. A threshold selection method from gray-level histograms. IEEE Trans. Syst. Man Cybern. 9 (1), 62–66.
Palanca, M., Cristofolini, L., Dall'Ara, E., et al., 2016. Digital volume correlation can be used to estimate local strains in natural and augmented vertebrae: an organ-level study. J. Biomech. 49 (16), 3882–3890.
Palanca, M., Tozzi, G., Cristofolini, L., et al., 2015. Three-dimensional local measurements of bone strain and displacement: comparison of three digital volume correlation approaches. J. Biomech. Eng. 137 (7).
Peña Fernández, M., Cipiccia, S., Dall'Ara, E., et al., 2018. Effect of SR-microCT radiation on the mechanical integrity of trabecular bone using *in situ* mechanical testing and digital volume correlation. J. Mech. Behav. Biomed. Mater. 88, 109–119.
Peña Fernández, M., Hoxha, D., Chan, O., et al., 2020. Centre of rotation of the human subtalar joint using weight-bearing clinical computed tomography. Sci. Rep. 10 (1), 1035.
Pistoia, W., van Rietbergen, B., Lochmüller, E.-M., et al., 2002. Estimation of distal radius failure load with micro-finite element analysis models based on three-dimensional peripheral quantitative computed tomography images. Bone 30 (6), 842–848.
Pugh, J.W., Rose, R.M., Radin, E.L., 1973. Elastic and viscoelastic properties of trabecular bone: dependence on structure. J. Biomech. 6 (5), 475–485.
Radhakrishnan, P., Lewis, N.T., Mao, J.J., 2004. Zone-specific micromechanical properties of the extracellular matrices of growth plate cartilage. Ann. Biomed. Eng. 32 (2), 284–291.

Radin, E.L., Rose, R.M., 1986. Role of subchondral bone in the initiation and progression of cartilage damage. Clin. Orthop. Relat. Res. 213, 34.
Rajalekshmi, R., Agrawal, D.K., 2025. Advancing osteoarthritis research: insights from rodent models and emerging trends. J. Orthop. Sports Med. 7 (1), 110–128.
Razi, H., Birkhold, A.I., Zaslansky, P., et al., 2015. Skeletal maturity leads to a reduction in the strain magnitudes induced within the bone: a murine tibia study. Acta Biomater. 13, 301–310.
Ren, P., Niu, H., Gong, H., et al., 2018. Morphological, biochemical and mechanical properties of articular cartilage and subchondral bone in rat tibial plateau are age related. J. Anat. 232 (3), 457–471.
Renders, G.a.P., Mulder, L., Langenbach, G.E.J., et al., 2008. Biomechanical effect of mineral heterogeneity in trabecular bone. J. Biomech. 41 (13), 2793–2798.
Renders, G.a.P., Mulder, L., van Ruijven, L.J., et al., 2011. Mineral heterogeneity affects predictions of intratrabecular stress and strain. J. Biomech. 44 (3), 402–407.
Ries, C., Boese, C.K., Stürznickel, J., et al., 2020. Age-related changes of micro-morphological subchondral bone properties in the healthy femoral head. Osteoarthr. Cartil. 28 (11), 1437–1447.
Roach, G.C., Edke, M., Griffin, T.M., 2012. A novel mouse running wheel that senses individual limb forces: biomechanical validation and in vivo testing. J. Appl. Physiol. 113 (4), 627–635.
Roach, H.I., Mehta, G., Oreffo, R.O.C., et al., 2003. Temporal analysis of rat growth plates: cessation of growth with age despite presence of a physis. J. Histochem. Cytochem. 51 (3), 373–383.
Roberts, B.C., Perilli, E., Reynolds, K.J., 2014. Application of the digital volume correlation technique for the measurement of displacement and strain fields in bone: a literature review. J. Biomech. 47 (5), 923–934.
Roemhildt, M.L., Coughlin, K.M., Peura, G.D., et al., 2006. Material properties of articular cartilage in the rabbit tibial plateau. J. Biomech. 39 (12), 2331–2337.
Ruffoni, D., William Chapman Dunlop, J., Fratzl, P., et al., 2010. Effect of minimal defects in periodic cellular solids. Philos. Mag. 90 (13), 1807–1818.
Ruffoni, D., van Lenthe, H., 2017. Finite Element Analysis in Bone Research: a Computational Method Relating Structure to Mechanical Function [Internet]. Elsevier [cited 2025 Nov 11]. Available from: https://orbi.uliege.be/handle/2268/212477.
Rummler, M., van Tol, A., Schemenz, V., et al., 2024. The lacunocanalicular network is denser in C57BL/6 compared to BALB/c mice. Calcif. Tissue Int. 115 (5), 744–758.
Ryan, M.K., Oliviero, S., Costa, M.C., et al., 2020. Heterogeneous strain distribution in the subchondral bone of human osteoarthritic femoral heads, measured with digital volume correlation. Materials 13 (20), 4619.
Sergerie, K., Lacoursière, M.-O., Lévesque, M., et al., 2009. Mechanical properties of the porcine growth plate and its three zones from unconfined compression tests. J. Biomech. 42 (4), 510–516.
Shipov, A., Zaslansky, P., Riesemeier, H., et al., 2013. Unremodeled endochondral bone is a major architectural component of the cortical bone of the rat (*Rattus norvegicus*). J. Struct. Biol. 183 (2), 132–140.
Stewart, H.L., Kawcak, C.E., 2018. The importance of subchondral bone in the pathophysiology of osteoarthritis. Front. Vet. Sci. 5, 178.
Tanoto, H., Fan, H., Ha, D., et al., 2024. Quantifying the relation between aging-related trabecular bone microstructure and mechanical properties with digital volume correlation approach. Extreme Mech. Lett. 73, 102265.
Tits, A., Blouin, S., Rummler, M., et al., 2023. Structural and functional heterogeneity of mineralized fibrocartilage at the achilles tendon-bone insertion. Acta Biomater. 166, 409–418.
Tozzi, G., Dall'Ara, E., 2025. An overview of reliable and representative DVC measurements for musculoskeletal tissues. J. Microsc. 300 (1), 3–17.
Turunen, M.J., Le Cann, S., Tudisco, E., et al., 2020. Sub-trabecular strain evolution in human trabecular bone. Sci. Rep. 10 (1), 13788.
Turunen, M.J., Saarakkala, S., Helminen, H.J., et al., 2012. Age-related changes in organization and content of the collagen matrix in rabbit cortical bone. J. Orthop. Res. 30 (3), 435–442.
Upload — BoneDVC [Internet]. [cited 2025 Dec 25]. Available from: https://bonedvc.insigneo.org/dvc/upload/. .
van Rietbergen, B., Ito, K., 2015. A survey of micro-finite element analysis for clinical assessment of bone strength: the first decade. J. Biomech. 48 (5), 832–841.
Villemure, I., Stokes, I.A.F., 2009. Growth plate mechanics and mechanobiology. A survey of present understanding. J. Biomech. 42 (12), 1793–1803.
Wang, J.-Y., Qi, Y.-S., Bao, H.-R.-C., et al., 2021. The effects of different repair methods for a posterior root tear of the lateral meniscus on the biomechanics of the knee: a finite element analysis. J. Orthop. Surg. Res. 16 (1), 296.
Xie, L., Lin, A.S.P., Levenston, M.E., et al., 2009. Quantitative assessment of articular cartilage morphology via EPIC-microCT. Osteoarthr. Cartil. 17 (3), 313–320.
Yamada, K., Healey, R., Amiel, D., et al., 2002. Subchondral bone of the human knee joint in aging and osteoarthritis. Osteoarthr. Cartil. 10 (5), 360–369.
Zanjani-Pour, S., Giorgi, M., Dall'Ara, E., 2020. Development of subject specific finite element models of the mouse knee joint for preclinical applications. Front. Bioeng. Biotechnol. 8, 558815.
Zauel, R., Yeni, Y.N., Bay, B.K., et al., 2005. Comparison of the linear finite element prediction of deformation and strain of human cancellous bone to 3D digital volume correlation measurements. J. Biomech. Eng. 128 (1), 1–6.
Zwahlen, A., Christen, D., Ruffoni, D., et al., 2015. Inverse finite element modeling for characterization of local elastic properties in image-guided failure assessment of human trabecular bone. J. Biomech. Eng. [Internet] 137 (11012) [cited 2026 Jan 20].
Zysset, P.K., 2003. A review of morphology–elasticity relationships in human trabecular bone: theories and experiments. J. Biomech. 36 (10), 1469–1485.
Zysset, P.K., Dall'Ara, E., Varga, P., et al., 2013. Finite element analysis for prediction of bone strength. BoneKEy Rep. 2, 386.